Implementation of consistent embedding for a larger system–Amorphous silica

KRISHNA MURALIDHARAN[a,*], ADITI MALLIK[b], KEITH RUNGE[a] and P.A. DEYMIER[c]

[a]*Quantum Theory Project, Departments of Physics and of Chemistry, University of Florida, Gainesville, FL 32611, USA*

[b]*Process Technology Modeling, Intel Corporation, Ronler Acres 3, 2501 NW 229 Avenue, Hillsboro, OR 97124, USA*

[c]*Department of Materials Science and Engineering, The University of Arizona, Tucson, AZ 85721, USA*

Abstract. We examine the performance and behavior of the consistent embedding multi-scale simulation techniques described in the preceding article. The test is bulk amorphous silica, primarily in the small-strain regime. We also examine some practical issues that arise when the technique is used to model mechanical failure. For context, we present results of classical molecular dynamics simulations of fracture mechanisms of amorphous silica.

1. Introduction

In the preceding two articles, we have presented an approach to concurrent multi-scale modeling that we call *consistent embedding*. In this contribution we examine the performance of this style of modeling in an amorphous silica system comprised of a few thousand atoms. While we aspire to the complete description of failure in this system, here we present a set of results that demonstrate that our procedure is sound for the small strain behavior of an amorphous system. For context, we also present a brief review of molecular dynamics (MD) simulations of failure of silica glass using the modified version of the BKS potential discussed in detail in the first article of this section. We also give some selected results which are indicative of the sorts of system characteristics that we will use our more detailed consistent embedding procedure to either confirm or modify.

Although we will compare the results of two simulations here, we remark that comparisons of simulations with experiment present their own difficulties. In experiment, amorphous silica usually is made by cooling a silica melt slowly until the glass forms. Although numerous procedural details can be controlled, the basic process is the cooling of a liquid. The time scale for this cooling can range from seconds through minutes, hours, or days, depending upon experimentally available quenching rates. In MD simulations, times that are routinely accessible are in the range

---

*To whom correspondence should be addressed, E-mail: krishna@qtp.ufl.edu

of picoseconds to nanoseconds, so that replication of the experiment in a simulation environment is computationally intractable. However, simulation techniques have been developed to address this challenge.

There is also a good deal of variability in amorphous systems which is not present in crystalline systems. A single crystal of α-quartz, for instance, has well-defined lattice constants, unit cells, and periodic structure. Whereas every α-quartz crystal is unambiguously constructed based on state variables (providing that we neglect environmental effects), any given sample of amorphous silica is structurally distinct. The challenge for the simulation is then to create a model sample that is structurally consistent with its experimental counterpart based on measurable characteristics.

Diverse procedures have been published for the construction of a simulated glass. We use the procedure of Huff et al. [1] as discussed in some detail in the first article of this collection. In brief, the amorphous system is created by beginning with the structure of β-crystobalite. That choice is motivated by the fact that the density of β-crystobalite is similar to that of silica glass. This sample, with periodic boundary conditions, then is run in MD while subjected to an annealing schedule. Beginning with a temperature much higher than the melting point of the simulated glass the simulation is held at that temperature to destroy the "memory" of the original structure. Then the temperature of the sample is reduced in steps until room temperature is reached. Finally, the sample is equilibrated at constant pressure to find its own metastable state. Having obtained an amorphous system, we must compare its structural characteristics with the experimental glass. To do so, we calculate the density, radial distribution function (RDF), and bond angle distributions (BAD) and compare with the available experimental data.

Establishing the initial state is only one way in which MD simulations differ from experiments. Another significant difference is the method of application of strain to the system. Experimental strain generally is introduced by fixing two portions of the sample which then are pulled apart to strain the system at a stipulated rate. In the preceding article, this procedure was simulated by fixing the vertical component of the positions of the end caps of a silica nano-rod. In a simulation, such as the present one, that uses periodic boundary conditions (PBC), this mode of strain application is not possible. We must employ a different procedure. Thus, we introduce strain homogeneously by scaling the coordinate, say z, along which the strain is applied, resulting in uniaxial homogeneous strain throughout the material. Clearly, as we have redefined how strain is incorporated, the definition of stress also must be reconsidered. Rather than using the mechanical definition of stress (i.e. the normal force per unit area), we invoke the virial theorem [2] to calculate the instantaneous internal stress response to the applied strain, specifically

$$\sigma_{mn} = \frac{1}{V} \sum_{i=1}^{N} (m_i v_{im} v_{in} + r_{in} F_{im}),$$

where m and n index cartesian directions, σ_{mn} is the corresponding stress tensor, V is the sample volume, N is the number of atoms, m_i, v_i, r_i and F_i represent the mass, velocity vector, position vector and force vector for the ith atom.

With a clearly defined protocol for preparing and straining the simulation samples, we are positioned to examine the behavior of the BKS glass that was introduced in

the first article of this section. One motivation for this discussion is to point out that interesting phenomena are accessible from MD simulations. Some of these characteristics can be compared directly to experimental results, particularly properties and trends. Other characteristics have no experimental counterpart, for example, mechanistic details. While we do not maintain that the BKS glass results should stand alone, work done on this system illustrates what can be examined using the consistent embedding procedures we have developed and described. In particular, we can assess the consequences of re-parameterizing the BKS potential form to match an embedded quantum mechanical (QM) method. In the third part of this paper, we present some preliminary results from the embedding procedure proposed in the preceding article. Finally, we draw some conclusions about the robustness of the embedding and its implications for multi-scale modeling.

2. The BKS glass

This section presents results of studies of the effects of uniaxial strains on the BKS glass. With that for context, we also survey results [3, Muralidharan et al. (Submitted)] regarding the atomic-scale mechanisms that control the failure process of silica glass using the modified BKS potential discussed in the first article of this collection.

With the annealing procedure described above and a cooling rate of 125 K/ps, we prepared samples of amorphous silica containing 3528 atoms (with PBC) with a density of 2.27 g/cm^3. The densities of all the simulated glass samples are in good agreement with the experimental result. Next, we applied strain rates from 0.1 / to 0.005/ps to the BKS sample and examined the atomic-level processes that characterize the failure process. The system parameters that were considered included the RDFs, BADs, and coordination of atoms as a function of increasing strain and their correlation to the overall stress response of the sample. In addition, we studied the growth of nano-scale and sub-nano-scale voids as a function of strain. This documentation was a very useful tool in characterizing the fracture process at a larger-than-atomic scale. The evolution of big voids with strain was noted; there was a systematic growth of some critical voids that could be correlated to the stress response of the material as shown in the following discussion.

Figure 1(a) depicts the stress–strain curves for the BKS glass for various strain rates and Figure 1b shows the evolution of the biggest void as a function of strain. From the former figure it is evident that the fracture strength of the material increases with increasing strain rate. Each stress–strain curve and the corresponding growth of the biggest void can be divided into three primary regions as shown in Figure 1a and b. In region I, the Si–O bonds (and the voids) are deformed elastically and the material responds to the applied strain elastically. Region II is characterized by a lack of variation in stress with increasing strain, a decrease in the rate of growth of the bigger voids, and breakage of some Si–O bonds which leads to the formation of singly coordinated (1-C) Oxygen and tri-coordinated (3-C) Silicon atoms. In region III, there is extensive atomic rearrangement that results in the formation of edge-sharing two-membered silica (2-M) rings in and around some voids that grow at the expense of others. There is a symbiotic growth of these voids and the surrounding 2-M rings via a two-step feedback mechanism, which consists of (i) atomic rearrangement and restructuring on and around the surface of a void, and (ii) growth of
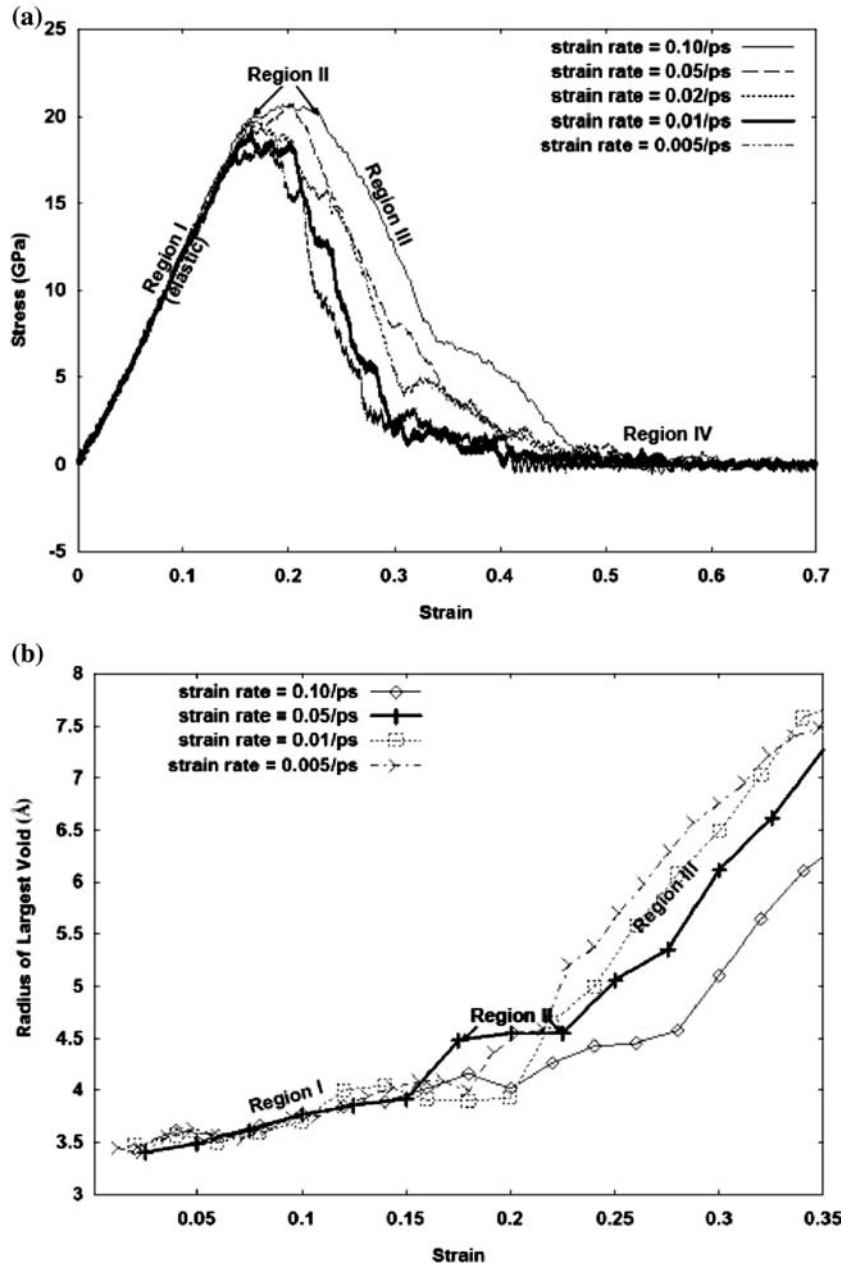
Figure 1. (a) Uniaxial stress–strain curves for BKS glass sample. (b) Growth of the biggest void at different strain rates for the BKS glass sample.

the void via rejection of volume that occurs due to local restructuring. The reduction of stress in region III arises from bulk recovery in the rest of the material. Finally, the material separates when critical voids form an interconnected network or a single critical void grows, such that the length of the void(s) extends across the dimensions that are perpendicular to the uniaxial strain direction of the material. This leads to the formation of two sub-materials, whose surface structure is vastly different from
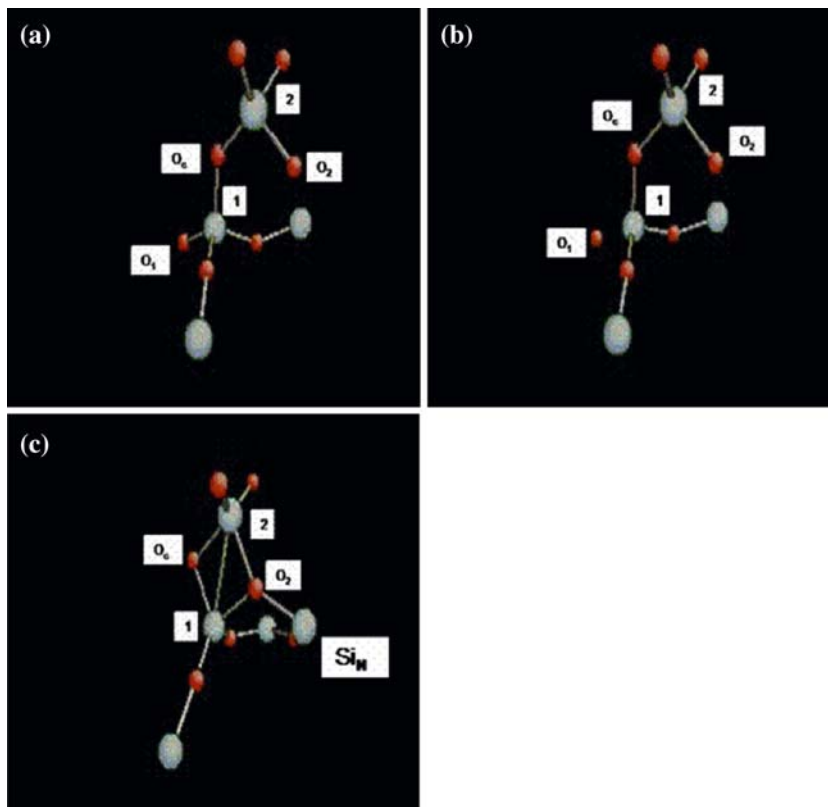
Figure 2. a–c Snapshot of the local structure of the BKS glass when subjected to a strain rate = 0.01/ps. The red atoms are Oxygens, blue are Silicons.

the bulk structure. Since the formation of the 2-M rings is critical to the fracture process, we give it more detailed consideration in the following discussion.

For this more detailed look at the fracture mechanism we restrict our discussion to a single strain rate. Figure 2a–c show the evolution of local structure in BKS glass when subjected to a strain rate of 0.01 /ps. For the sake of specificity, we track two neighboring silica tetrahedra that initially share a common Oxygen atom and later form a 2-M ring.

Figure 2(a) shows two Si atoms–labeled 1 and 2 – that share a common corner-sharing Oxygen atom (O_c). With increasing strain, Si (1) loses one of its Oxygen neighbors (O_1) as shown in Figure 2b (we define a Si atom and an O atom to be neighbors if their separation is less than 2 Å). Rapidly, within a strain increment of 0.01, the bond distance between Si (1) and O_1 goes from 1.78 Å to 2.23 Å, and then within the next successive 0.01 strain increment, the separation becomes more than 3.5 Å, with large kinetic energies being imparted to each of the two atoms. This results in Si (1) being temporarily 3-C until it acquires O_2 as a neighbor to make it 4-C again, thus forming the 2-M ring (Figure 2c). As the 2-M ring is formed, O_2 becomes 3-C, with its neighbors being Si (1), Si (2), and Si_N see Figure 2(c). Before the formation of the 2-M ring, O_2 was coordinated only to Si_N and Si (2).

Having summarized the important mechanisms leading to the fracture process in amorphous silica, we turn our attention towards understanding thermal effects and defect concentration effects on the fracture process. We begin by examining the fracture behavior of the BKS glass at 300, 1000, and 2000 K at the relatively fast and slow strain rates of 0.05/ps and 0.005/ps. Figure 3 shows the initial Si–O RDF for these three temperatures. Note that the distribution spreads as the temperature increases as one would expect. At the higher strain rate, there is a decrease in the
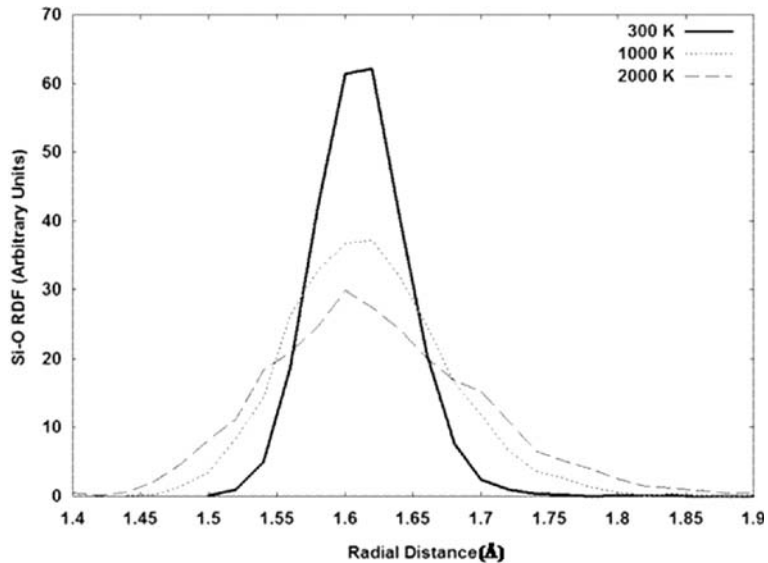

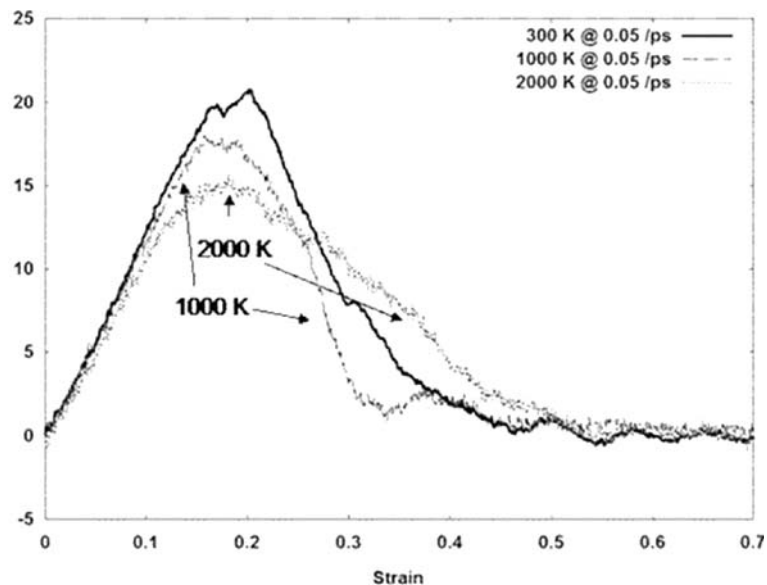*Figure 3.* Initial Si–O radial distribution function for BKS glass at three temperatures.

Figure 4. Uniaxial stress–strain curves for the BKS glass at different temperatures with a strain-rate of 0.05/ps.
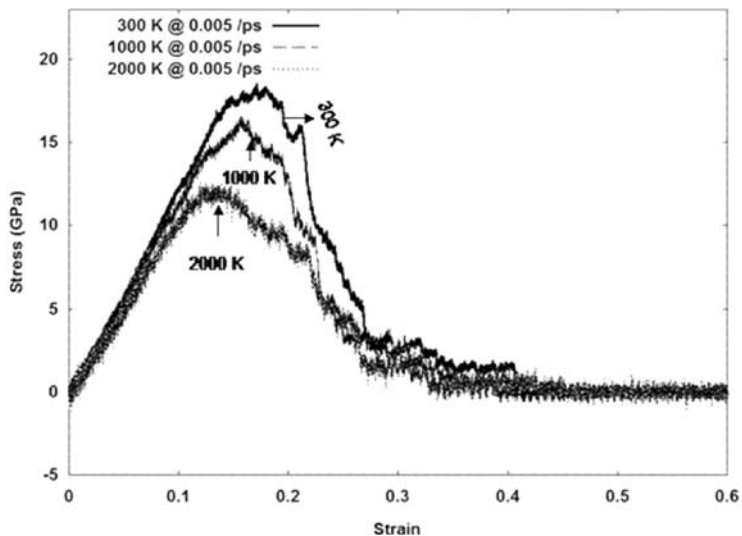
Figure 5. Uniaxial stress–strain curves for the BKS glass at different temperatures with a strain-rate of 0.005/ps.
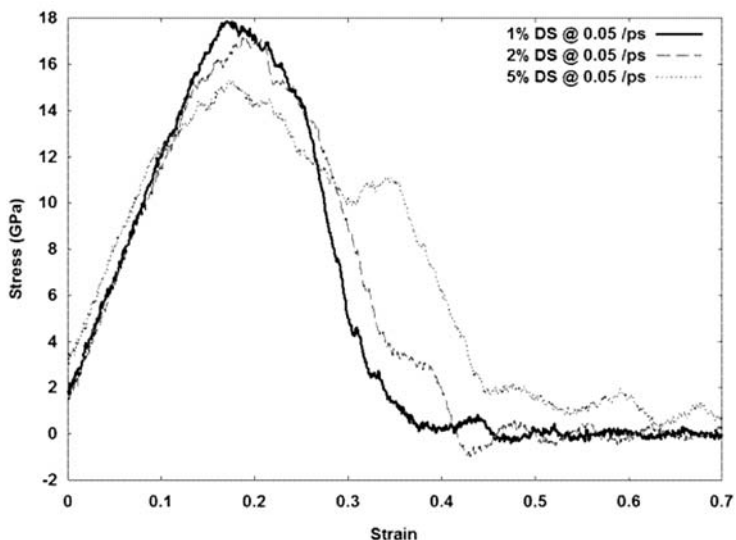

Figure 6. Uniaxial stress–strain Curves (at 0.05/ps) for select defective glasses at 300 K.

maximum stress in the sample as temperature increases (see Figure 4). The width of region II, the region of flow, appears to grow with increased temperature as is most clearly evident at 2000 K. At the lower strain rate, the decrease in maximum stress as a function of increased temperature is again evident. The increase in flow is now most prevalent at 300 K due to the occurrence of the onset of region II at lower strain values at the higher temperature (Figure 5).

We have introduced defects into the BKS glass by random removal of atoms from the amorphous sample that maintains the appropriate Si:O ratio. Three defect concentrations were considered, 1, 2, and 5%. Figure 6 presents the stress-strain curves

Table 1. Densities of the different glasses

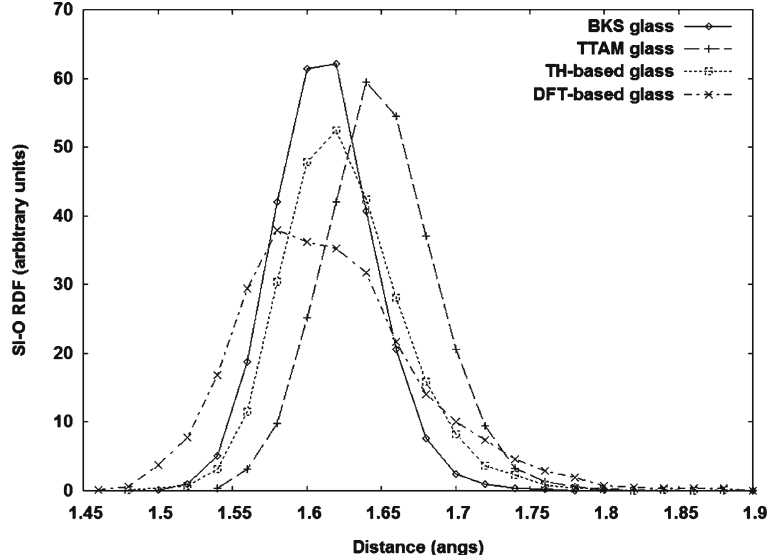| Glass	BKS	TTAM	TH-based	DFT based
Density(g/cc)	2.28	2.21	2.40	2.24

Figure 7. Short ranged Si–O RDFs of the different glasses.

for these three "defected samples" (DS). We note that the introduction of defects reduces the maximum stress of the system by at least 10%. The lower defect concentrations lead to stress–strain curves that have flow over about the same increment of strain as in the defect-free case. For the 5% DS, the maximum stress is the lowest and the increment of strain over which flow occurs is somewhat larger than in the other DS and defect-free cases. It is of interest to examine whether these qualitative observations are confirmed by the result obtained when using consistent embedding.

3. Consistent embedding

The preceding article introduced the concept of consistent embedding and illustrated it with detailed examination of a small system. Here we investigate the issues that arise when this technique is applied to a larger system, namely silica glass. As a first step, we consider the TH-based re-parameterization (described in the preceding article). The annealing schedule and cooling rate to prepare the samples were the same as described above. Although the parameterization of the TH-based potential was carried out on a silica nano-rod, hence involved no information about bulk systems, we obtained bulk silica glasses (2940 atoms) with properties comparable to the BKS and TTAM glasses. The TH-based glass is slightly denser (see Table 1). It also lists the density of a glass modeled via a DFT-based re-parameterization (also discussed in that preceding article). Comparisons of the short-range Si–O RDFs and the Si–O–Si and O–Si–O BADs of the different glasses are shown in Figure 7 and Figure 8.
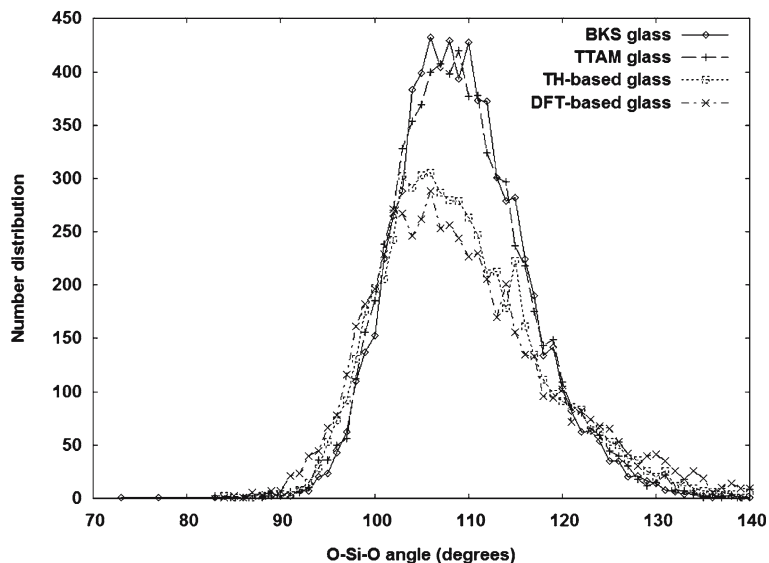
Figure 8. O–Si–O BAD of the different glasses.

3.1. EMBEDDING METHODOLOGY

Before embarking on a full-blown consistent embedding simulation to model failure, there are many issues that have to be addressed. These include the dynamic identification of domains in the silica glass that are relatively weaker than the rest of the material, hence are candidates for the eventual region of failure. Our work on such domain identification is elaborated in the first article of this section. Therefore we only discuss other pertinent issues in the rest of this article.

In multi-scale simulations that involve coupling quantum mechanical methods with classical atomistic simulations such as our consistent embedding method, the inter-atomic potential used to represent interactions in the atomistic simulations must, at least, reflect the quantum method characteristics for small strain response. Specifically in our method, if the initial elastic responses of both embedded and embedding regions are not similar, then there would be a significant mismatch leading to an artificial introduction of strain in one of the two regions (explained in detail in the first article of this section). The difficulty would be evident even when the coupled material is equilibrated under strain-free conditions. So, as a first step, using the TH to represent the embedded region and the TH-based potential to represent the embedded region, we carried out zero-strain trial equilibration runs on amorphous silica samples (prepared using the TH-based potential with 2940 atoms) at 300 K with the temperature controlled via a Nosé–Hoover thermostat [4].

Since our simulations involve examining the dynamics of the coupled material at zero strain, we did not invoke the domain identifier, but instead arbitrarily carved out cubic sub-sections in the material as our embedded regions and carried out the simulations for many such regions one at a time. Typically each embedded region had from 60 to 150 atoms; see discussion below. In a fashion similar to that of the preceding article, we terminated the embedded region with pseudo-atoms. Pseudo-atom identification was via a coordination criterion, as follows. Initially, we identified all

Table 2. Comparison of properties of composite glasses as a function of embedded domain size.

System	Volume ($\mathring{A}^3$)	Average Si–O distance ($\mathring{A}$)	Average O–Si–O angle (degrees)	Average Si–O–Si angle (degrees)	Initial number of embedded/pseduo-atoms
Bulk	–	1.64	105.5	148.0	–
Domain I	1980	1.65	110.0	155.4	165/40
Domain II	1400	1.65	109.4	155.0	102/37
Domain III	735	1.65	109.5	154.0	78/37
Domain IV	588	1.65	109.0	153.0	63/30

the Si atoms inside the carved out region. Next, we identified the neighbors of a given Si atom in that set to be all O atoms within a 2.0 Å radius. Any of the identified O atoms which had any Si neighbors not in the carved-out region then were designated to become pseudo-atoms.

The forces on the embedded atoms were calculated via the TH, while the classical forces on the rest of the atoms (including pseudo-atoms) were calculated via the TH-based potential. Note that forces on the atoms in the embedding region include both columbic (via the Ewald summation [5] and non-columbic interactions with the embedded atoms (or their periodic images). The embedding atoms are considered to be point charges (recall preceding article), and the net dipole due to these atoms becomes an input for the TH.

3.2. Results for the equilibration runs

Ideally, at zero strain, the embedding and embedded regions in the coupled material should be consistent with one another and there should be no induced strain in either region. Recall from the preceding article that the classical potential parameterized to the TH is accurate to a few percent in properties of interest, including the forces. Hence, there can be a slight mismatch in the forces at the boundary of the QM region. We must investigate both the severity and ramifications of such an imbalance in our treatment. In the preceding article we showed that the slight mismatch had no negative impact on the description of the model system (nano-rod). We need to do a similar assessment in our target system.

The use of a mixed-potential method for MD of the sort developed for our consistent embedding also has implications for the sort of MD ensembles that may be considered. For example, the composite system is not strictly conservative in that values of the system energy arise differently from the QM and CM regions. The implication is that simulating a NVE/NPE ensemble (i.e. a constant energy simulation, with N, the total number of atoms, E, the energy, V, the volume, and P, the pressure) may not be possible in the traditional ways.

As this is our first test of the embedding in the target system at zero strain, we equilibrated the coupled material (with arbitrarily identified domains) for 1.0 ps at 300 K, with a 1 fs MD time step. During equilibration, embedded atoms were identified dynamically by their locations. We repeated this procedure for a few different locations and sizes of the embedded zone, such that each trial zone had a different number of atoms. Although in principle one could use the TH method to evaluate the forces on all atoms in a given domain irrespective of domain size, given the
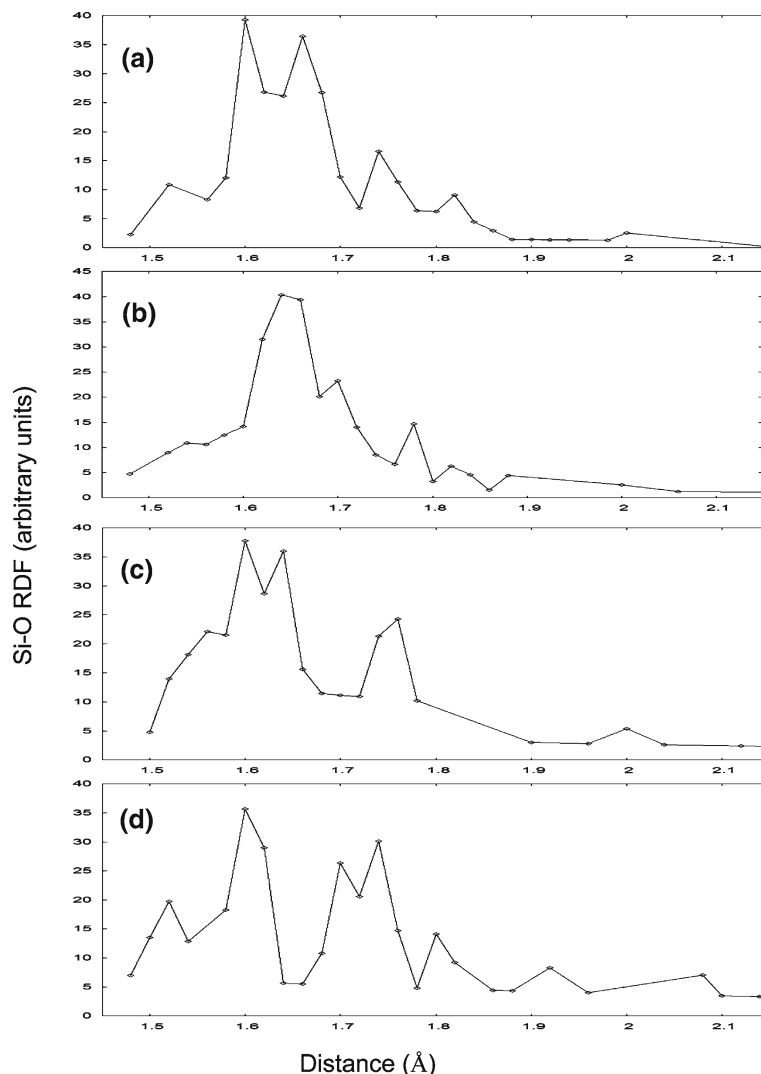
Figure 9. Equilibrated first-neighbor Si–O RDF for composite with (a) domain I, b) domain II, (c) domain III, and (d) domain IV.

disordered structure of the silica glass we dealt with domains containing as many as 165 embedded atoms (excluding pseudo-atoms). We now present results that examine the degree of force matching between the two domains for four different sizes of the embedded domain.

Table 2 gives the size of each embedded domain, the initial number of embedded and pseudo-atoms, the average equilibrated first-neighbor Si–O distance within the embedded region, and the average equilibrated Si–O–Si and O–Si–O BADs. Also for comparison, we have tabulated the bulk (i.e. TH-based potential glass) average Si–O bond distance as well as the bulk Si–O–Si and O–Si–O BADs. From Table 2 it is obvious that average Si–O–Si and O–Si–O BADs for all four composite cases are larger than their bulk counterparts, while the average Si-O distance in the embedded region is very similar to bulk. Figure 9, which displays the Si–O first neighbor
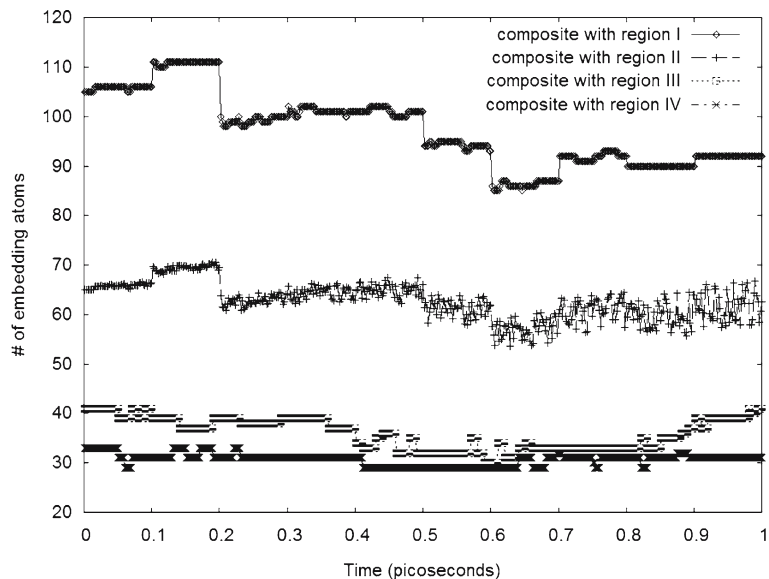
Figure 10. Number of embedded atoms as a function of time for the different composites.
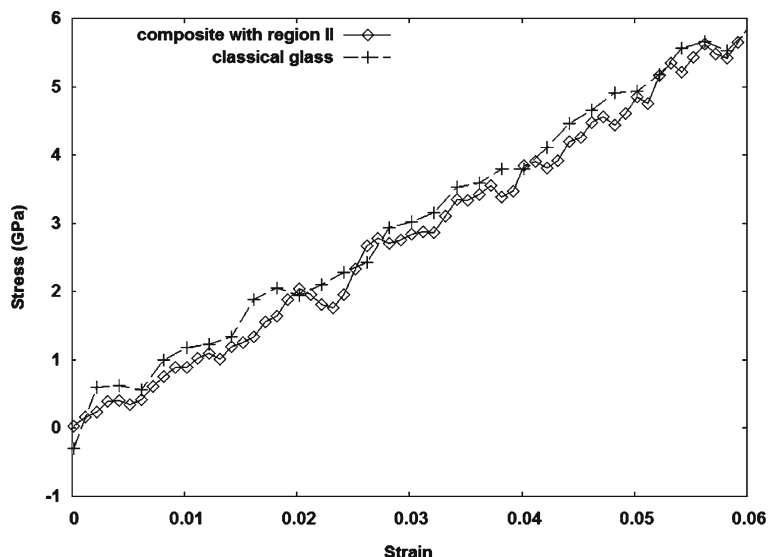

Figure 11. Stress-strain curve for target system with quantum domain 2.

RDF's functions for the four equilibrated composite samples, shows the role of quantum chemistry in emphasizing the tetrahedral structure of Si–O clusters in the embedded domains. Recall that in the BKS–style classical potential there is no term that enforces this structure. Rather, it seems that the large charges attributed to the ions tend to force the system toward tetrahedral structure. As we have defined the QM domain by its spatial coordinates in this initial investigation, there is a slight rearrangement of atoms between QM and CM domains for each of our four equilibration runs. Clearly, this redistribution of atoms could be prevented if we were to define the QM domain initially by its ions and associated electrons as in the preceding

article. The change in the number of QM domain atoms, as shown in Figure. 10, also demonstrates that we are capable of identifying cut bonds at any time step in the MD simulation, as will be demanded in on-the-fly simulations of our target system taken to failure. Figure 11 demonstrates the indistinguishability of the small-strain response of the full system and the composite system with a significant number of atoms included in the QM domain, labeled domain II.

These results demonstrate that our consistent embedding, trained in the previous article on a model system, performs as desired in the substantially larger target system.

Acknowledgements

References

1. Huff, N.T., Demiralp, E., Cagin, T., Goddard W.A., III, J. Non-Cryst. Solids, 253 (1999) 133.
2. Gibbs, J., Trans. Connect. Acad, 2, (1873) 311.
3. Muralidharan, K., Simmons, J. H., Deymier, P. A., Runge, K., J. Non-Cryst. Solids, 351 (2005) 1532.
4. Hoover, W.G., Phys. Rev. A, 31, (1985)1695; Nosé, S., Mol. Phys., 52, (1984) 255.
5. Ewald, P., Annln. Phys, 64 (1921) 253.